

MATERIALS SCIENCE

Discovery of Lorentz-violating type II Weyl fermions in LaAlGe

Su-Yang Xu,^{1*} Nasser Alidoust,^{1,2*} Guoqing Chang,^{3,4*} Hong Lu,^{5*} Bahadur Singh,^{3,4*} Ilya Belopolski,¹ Daniel S. Sanchez,¹ Xiao Zhang,⁵ Guang Bian,^{1,6} Hao Zheng,¹ Marios-Adrian Husanu,^{7,8} Yi Bian,⁵ Shin-Ming Huang,^{3,4,9} Chuang-Han Hsu,^{3,4} Tay-Rong Chang,^{10,11} Horng-Tay Jeng,^{10,12} Arun Bansil,¹³ Titus Neupert,¹⁴ Vladimir N. Strocov,⁷ Hsin Lin,^{3,4} Shuang Jia,^{5,15} M. Zahid Hasan^{1†}

2017 © The Authors, some rights reserved; exclusive licensee American Association for the Advancement of Science. Distributed under a Creative Commons Attribution NonCommercial License 4.0 (CC BY-NC).

In quantum field theory, Weyl fermions are relativistic particles that travel at the speed of light and strictly obey the celebrated Lorentz symmetry. Their low-energy condensed matter analogs are Weyl semimetals, which are conductors whose electronic excitations mimic the Weyl fermion equation of motion. Although the traditional (type I) emergent Weyl fermions observed in TaAs still approximately respect Lorentz symmetry, recently, the so-called type II Weyl semimetal has been proposed, where the emergent Weyl quasiparticles break the Lorentz symmetry so strongly that they cannot be smoothly connected to Lorentz symmetric Weyl particles. Despite some evidence of nontrivial surface states, the direct observation of the type II bulk Weyl fermions remains elusive. We present the direct observation of the type II Weyl fermions in crystalline solid lanthanum aluminum germanide (LaAlGe) based on our photoemission data alone, without reliance on band structure calculations. Moreover, our systematic data agree with the theoretical calculations, providing further support on our experimental results.

INTRODUCTION

In 1937, physicist Conyers Herring theoretically identified the conditions under which electronic bands in solids have the same energy and momentum in crystals that lack inversion symmetry (*1*). Near these band touching points, the low-energy excitations, or electronic quasiparticles, can be described by an equation that is essentially identical to the Weyl equation (*2*). Although Herring referred to the degeneracies as “accidental,” recent advances in band theory have led to the understanding that they are topologically protected and realize a so-called Weyl semimetal (*1–9*). The quasiparticles in the vicinity of these nodes are emergent Weyl fermions. They behave like Berry curvature monopoles or anti-monopoles, depending on their respective chirality. The Weyl fermions of opposite chiralities are separated in momentum space. This electronic structure leads to a very special electromagnetic response and novel nonlocal transport phenomena (*10*) of the material. In parallel electric and magnetic fields, the apparent conservation of the chiral charge is broken by the chiral anomaly, making a Weyl metal, unlike ordinary nonmagnetic metals, more conductive with an increasing magnetic field (*11*). Because of these novel properties, Weyl semimetals

have the potential to be as important as graphene and topological insulators and have attracted worldwide interest.

Lorentz symmetry is the symmetry that requires physical laws to be independent of the frame of reference, in which they are observed (*12*). Hence, it is at the heart of any accepted physical theory, such as quantum field theory and Einstein’s theory of relativity, and has deep connections to the principle of causality and the charge, parity, and time-reversal symmetry (*13–15*). The search for Lorentz violation is one of the central themes of modern high-energy physics because many of the theories beyond the standard model, with the intention of further incorporating gravity, violate Lorentz symmetry. To date, Lorentz symmetry has survived a century of tests and remained to appear exact. In high-energy physics, Weyl fermions travel at the speed of light and therefore strictly obey Lorentz symmetry. Despite its robustness in high-energy physics, Lorentz symmetry is not present in low-energy condensed matter physics because slow-moving emergent electronic quasiparticles in crystals generally break Lorentz symmetry. Several groups theoretically considered the Lorentz violating emergent Weyl fermions in various forms including tilted Weyl cones and, as a result, the condensed matter realization of the Lorentz violating quantum field theory in a Weyl semimetal (*16–19*). Recently, it was realized that if the Lorentz violation in a Weyl semimetal is strong enough, then the emergent quasiparticles should be regarded as a new type of Weyl fermions, which is named type II Weyl fermions (*19*). In conventional (type I) Weyl semimetals, the emergent Weyl fermions respect (or at least approximately respect) the Lorentz symmetry. Specifically, the small Lorentz breaking of the type I Weyl fermions can be adiabatically removed. Therefore, any type I Weyl fermion is smoothly connected to the Lorentz invariant Weyl fermion. The type I Weyl cone arises from the crossing between two bands that have velocities of opposite sign for any momentum direction, and the Fermi surface consists of zero-dimensional isolated points if the Fermi level is set at the energy of the Weyl nodes. Type I Weyl semimetals have been realized in the TaAs class of materials and a double-gyroid photonic crystal (*7–9*). Fermi arcs and Weyl fermions have been observed by spectroscopic experiments

¹Department of Physics, Laboratory for Topological Quantum Matter and Spectroscopy (B7), Princeton University, Princeton, NJ 08544, USA. ²Rigetti & Co Inc., 775 Heinz Avenue, Berkeley, CA 94710, USA. ³Centre for Advanced 2D Materials and Graphene Research Centre, National University of Singapore, 6 Science Drive 2, Singapore 117546, Singapore. ⁴Department of Physics, National University of Singapore, 2 Science Drive 3, Singapore 117542, Singapore. ⁵International Center for Quantum Materials, School of Physics, Peking University, Beijing, China. ⁶Department of Physics and Astronomy, University of Missouri, Columbia, MO 65211, USA. ⁷Paul Scherrer Institute, Swiss Light Source, CH-5232 Villigen PSI, Switzerland. ⁸National Institute of Materials Physics, 405A Atomistilor Street, 077125 Magurele, Romania. ⁹Department of Physics, National Sun Yat-Sen University, Kaohsiung 804, Taiwan. ¹⁰Department of Physics, National Tsing Hua University, Hsinchu 30013, Taiwan. ¹¹Department of Physics, National Cheng Kung University, Tainan 701, Taiwan. ¹²Institute of Physics, Academia Sinica, Nankang, Taipei 11529, Taiwan. ¹³Department of Physics, Northeastern University, Boston, MA 02115, USA. ¹⁴Department of Physics, University of Zurich, Winterthurerstrasse 190, CH-8052, Switzerland. ¹⁵Collaborative Innovation Center of Quantum Matter, Beijing 100871, China.

*These authors contributed equally to this work.

†Corresponding author. Email: mzhazan@princeton.edu

(7–9), and the negative magnetoresistance due to the chiral anomaly has been reported in transport experiments on the TaAs class (39, 40).

The novel type II Weyl fermions (19), in contrast, violate Lorentz symmetry so strongly that they cannot be smoothly connected back to the regular relativistic (Lorentz invariant) Weyl fermions (19–31). Such a type II Weyl fermion cone arises from the crossing between two bands that have the same sign of velocity along a certain direction. Its Fermi surface consists of an electron and a hole pocket that touch at the Weyl node in a topologically protected manner. Since the proposal of the concept of the type II Weyl fermions (19), there have been many theoretical works predicting specific new topological phenomena, including an exotic chiral anomaly whose transport response strongly depends on the direction of the electric current, an antichiral effect of the chiral Landau level, a modified anomalous Hall effect, magnetic breakdown, Klein tunneling, etc. (19, 26–31). These predicted phenomena can be detected in transport and spectroscopic experiments,

leading to protected properties that can be potentially used in future applications.

Because the type II Weyl fermion node is a touching point in the three-dimensional (bulk) Brillouin zone (BZ), it can only be shown by measuring the band structure along all three momentum space directions (k_x, k_y, k_z) (Figs. 1 and 2). To stress the importance of this experimental requirement, we compare two cases shown in Fig. 3 (J to M). In Fig. 3L, we show the Fermi surface of a type II Weyl semimetal where bulk electron and hole pockets touch to form the type II Weyl node. By contrast, in Fig. 3M, we have a trivial electron pocket and a trivial hole pocket without any Weyl nodes. They do not touch in the bulk BZ. These two cases can be clearly distinguished by measuring the band structure along all three momentum space directions (k_x, k_y, k_z). However, if one only has k_x and k_y resolution, then all bulk bands at different k_z values will be projected onto a single (k_x, k_y) plane. As shown in Fig. 3 (J and K), the two cases become

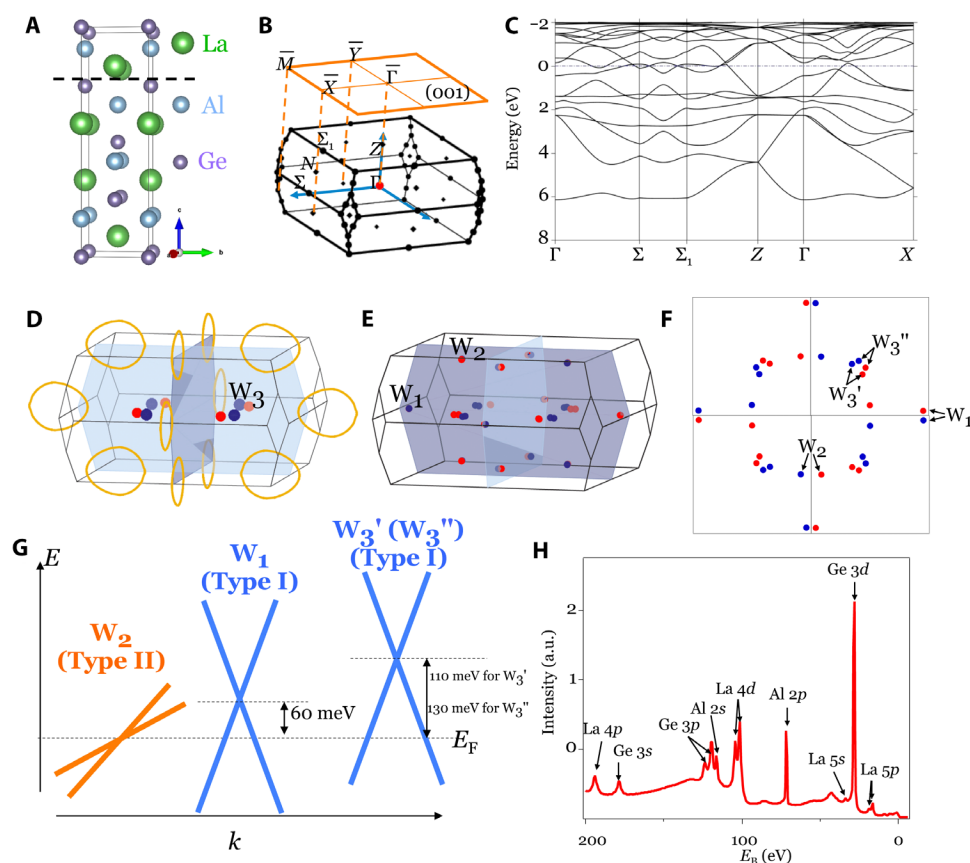


Fig. 1. Topology and BZ symmetry of LaAlGe. (A) Body-centered tetragonal structure of LaAlGe, with space group $I4_1md$ (109). The structure consists of stacks of La, Al, and Ge layers, and along the (001) direction, each layer consists of only one type of element. (B) The bulk and (001) surface BZ. (C) First-principles band structure calculations along high-symmetry directions without spin-orbit coupling (SOC). (D) Momentum space configuration of the four nodal lines (two on the $k_x = 0$ and two on the $k_y = 0$ mirror planes) denoted by the rings, as well as the four spinless pairs of Weyl nodes denoted as W_3 on the $k_z = 0$ plane, in the absence of SOC. Blue and red colors indicate positive and negative chiralities, respectively. (E) Configuration of the 40 Weyl nodes in the bulk BZ created upon the inclusion of SOC. The nodal lines are gapped out by SOC, and 24 Weyl nodes emerge in the vicinity of the nodal lines. In addition, each spinless W_3 Weyl node splits into two spinful Weyl nodes of the same chirality, which we denote as W_3' and W_3'' . Hence, the eight W_3 without SOC evolve into eight W_3' and eight W_3'' Weyl nodes with SOC. Therefore, in total, there are 40 Weyl nodes. For the 24 Weyl nodes that emerge from the gapping of the nodal line, we denote the 8 Weyl nodes that are near the boundaries of $k_z = 0$ plane as W_1 and the other 16 that are away from the $k_z = 0$ plane as W_2 . The W_3' and W_3'' are also on the $k_z = 0$ plane, but they are near the diagonal lines. (F) Projection of the Weyl nodes on the (001) surface BZ in one quadrant. (G) Schematics comparing the three types of Weyl nodes appearing upon the inclusion of SOC. The W_2 nodes are type II Weyl nodes, whereas the W_1, W_3' , and W_3'' nodes are type I. W_2 Weyl nodes are located almost exactly at the Fermi level, whereas W_1, W_3' , and W_3'' Weyl nodes are about 60, 110, and 130 meV above the Fermi level, respectively. (H) Core level measurement of the studied samples, which clearly shows the expected La, Al, and Ge peaks. a.u., arbitrary units.

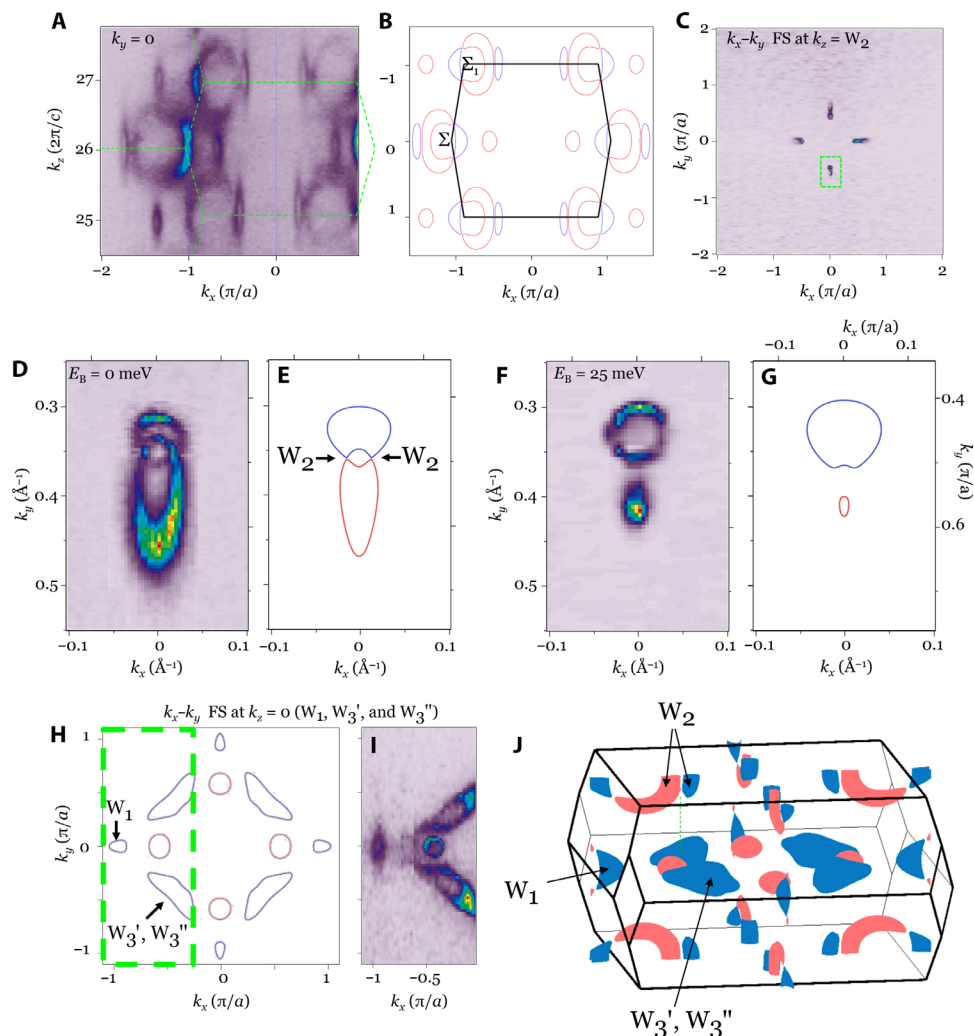


Fig. 2. Observation of type II Weyl nodes in LaAlGe. (A) High-energy soft x-ray ARPES (SX-ARPES) measurement and (B) first-principles calculation of $k_x - k_y$ Fermi surface maps at $k_y = 0$. The dashed green hexagon in (A) and the black hexagon in (B) correspond to the boundary of the first BZ on the $k_y = 0$ plane. The photon energies corresponding to the k_z values in (A) are between 320 and 600 eV. (C) SX-ARPES-measured $k_x - k_y$ Fermi surface map at k_y corresponding to the W_2 Weyl nodes. (D) Zoomed-in version of the measured and (E) calculated $k_x - k_y$ Fermi surface maps in the region marked by the green rectangle in (C). In the first-principles calculations, blue lines correspond to hole-like pockets, whereas red lines indicate electron-like pockets. (F and G) Same as (D) and (E) for a constant energy contour at 25 meV below the Fermi level. The photon energy used in the measurements presented in (C), (D), and (F) is 542 eV. (G and H) First-principles-calculated $k_x - k_y$ Fermi surface map at $k_z = 0$ (location of W_1 , W_3' , and W_3'' Weyl nodes), which shows the shapes of the pockets resulting from W_1 , W_3' , and W_3'' and other trivial pockets. (I) SX-ARPES-measured $k_x - k_y$ Fermi surface map at $k_z = 0$ in the region of the BZ denoted by the green dashed rectangle in (H). This experimentally observed Fermi surface map is in qualitative agreement with the calculated results presented in (H). The photon energy used here is 478 eV. (J) Calculated Fermi surface over the first bulk BZ. The pockets arising from the Weyl fermion cones are marked. Other pockets are trivial bulk bands. The red and blue colors denote electron- and hole-like pockets. Particularly, it can be seen that the W_2 node arises from the touching between electron and hole pockets, confirming their type II nature.

indistinguishable because the projected Fermi surface in both cases shows a crossing between the projected electron and hole pockets. This example highlights the importance of resolving the bulk band structure along all three momentum space directions for experimentally observing type II Weyl fermions. Further discussions regarding this issue can be found in section S4.

RESULTS

LaAlGe crystallizes in a body-centered tetragonal Bravais lattice, space group $I4_1md$ (109), C_{4v} point group. The lattice constants according to

previous diffraction experiments are $a = b = 4.336 \text{ \AA}$ and $c = 14.828 \text{ \AA}$ (41). The basis consists of two La atoms, two Al, and two Ge atoms, as shown in Fig. 1A. In this crystal structure, along the (001) direction, each atomic layer consists of only one type of element and is shifted relative to the layer below by half a lattice constant in either the x or y direction. This shift gives the lattice a screw pattern along the z direction, which leads to a nonsymmorphic C_4 rotation symmetry that includes a translation along the z direction by $c/4$. Figure 1C shows the calculated bulk band structure along high-symmetry lines without SOC. It can be seen that the conduction and valence bands cross each other along the $\Gamma - \Sigma - \Sigma_1$ path, demonstrating a semimetal ground state. The

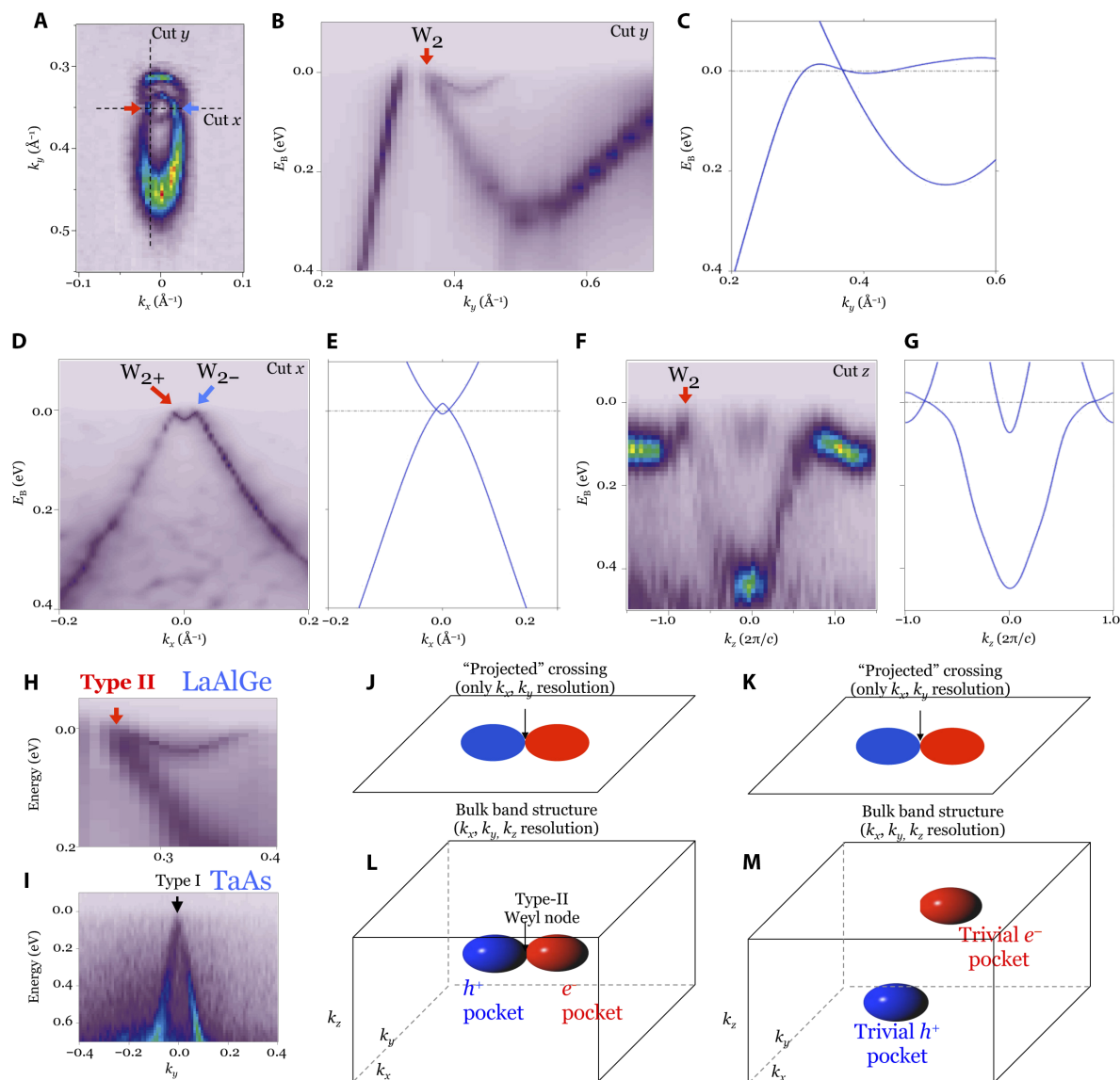


Fig. 3. Type II Weyl fermions in LaAlGe. (A) The $k_x - k_y$ Fermi surface map revealing a pair of type II W_2 Weyl nodes in the form of touching points between electron and hole pockets. (B) Measured and (C) calculated $E - k_y$ dispersion maps along the cut y direction denoted in (A), which clearly resolve the W_2 type II Weyl node at the crossing of two bands with the same sign of Fermi velocity. (D) Measured and (E) calculated $E - k_x$ dispersion maps for the direction along the cut x in (A). Here, the two type II W_2 Weyl cones with opposite chirality nodes are resolved simultaneously. The photon energy used in the measurements presented in (A), (B), and (D) is 542 eV. (F) Measured and (G) calculated $E - k_z$ dispersion maps along cut z , showing that the W_2 Weyl cone also disperses linearly along the out-of-plane k_z direction. (H and I) ARPES dispersion maps showing the difference between the type II Weyl fermions of LaAlGe and type I Weyl fermions of TaAs, respectively. (L) The Fermi surface of a type II Weyl semimetal where electron and hole pockets touch to form the type II Weyl node. (J) The projected Fermi surface shows a crossing between the projected electron and hole pockets. (M) We have a completely different scenario in the bulk. The electron and hole pockets are separated at different k_z values. (K) However, on the surface, their projections can still touch. This example clearly shows that the observation of a crossing in the projected band structure on surface does not mean a crossing in the bulk. The red and blue ellipsoids represent the electron and hole Fermi surfaces in the bulk BZ, respectively. The red and blue ellipses are the surface projection of the bulk Fermi surfaces.

momentum space configurations of the band crossings are shown in Fig. 1 (D and E). In the absence of SOC (Fig. 1D), the crossing between conduction and valence bands yields four closed loops, nodal lines on the $k_x = 0$ and $k_y = 0$ mirror planes, and also four pairs of (spinless) Weyl nodes on the $k_z = 0$ plane, which are denoted as W_3 in Fig. 1D. Upon the inclusion of the SOC (Fig. 1E), the nodal lines are gapped out, and 24 Weyl nodes emerge in the vicinity, which is similar to the case of TaAs (7). We refer to the 8 Weyl nodes located on the $k_z = 0$ plane as W_1

and the remaining 16 Weyl nodes away from this plane as W_2 . Moreover, when SOC is taken into account, each W_3 (spinless) Weyl node splits into two (spinful) Weyl nodes of the same chirality, which we call W_3' and W_3'' . Hence, in total, there are 40 Weyl nodes in a BZ, as shown in Fig. 1E. The projection of the Weyl nodes on the (001) surface BZ is shown in Fig. 1F. All W_1 Weyl nodes project as single Weyl nodes in close vicinity to the \bar{X} and \bar{Y} points on the surface BZ edges. Two W_2 Weyl nodes of the same chiral charge project onto the same

point near the midpoint of the $\Gamma - X$ and $\Gamma - Y$ lines. The W_3' and W_3'' nodes are projected near the midpoint of the $\Gamma - M$ (diagonal) lines. As schematically shown in Fig. 1G, which is drawn according to our calculation results, the W_2 Weyl fermions are of type II, whereas the W_1 , W_3' , and W_3'' Weyl fermions are of type I. All W_1 , W_3' , and W_3'' nodes are far away from the Fermi level in energy, whereas the W_2 nodes are located almost exactly at the Fermi level. Figure 1H shows the angle-integrated photoemission spectrum of LaAlGe over a wide range of binding energy. We identify the La $4p$, $4d$, $5s$; Al $2s$, $2p$; and Ge $3s$, $3p$, $3d$ core levels, confirming that our samples are composed of these three elements.

Below, we will focus on presenting our angle-resolved photoemission spectroscopy (ARPES) data on LaAlGe and show how these data demonstrate type II Weyl fermions without relying on the agreement with theoretical calculations. Figure 2A shows the measured $k_z - k_x$ Fermi surface contours of the bulk bands on the $k_y = 0$ plane. We observe large identical contours enclosing the Σ and Σ_1 points. In addition, we observe two small contours on the left- and right-hand sides of the big contour. These data unambiguously show that the observed band features are bulk bands rather than surface states by their definitions. A surface state is localized on the surface and therefore does not disperse along the k_z direction. By contrast, a bulk state is delocalized throughout the bulk and therefore disperses along the k_z direction with a period defined by bulk BZ. Our data in Fig. 2A show that the observed bands clearly have strong k_z dispersions. Even more decisively, the measured periodicity of the k_z dispersion matches the bulk BZ size along the k_z direction, which is defined by the lattice constant $c = 14.828$ Å, independently measured by x-ray diffraction (XRD). Therefore, these data unambiguously show that the observed band features are bulk bands.

Figure 2C shows the ARPES measured $k_x - k_y$ Fermi surface using incident photon energy 542 eV. We see that the Fermi surface consists of small pockets along the k_x and k_y axes. Figure 2D shows a high-resolution zoomed-in Fermi surface map of the region highlighted by the green box in Fig. 2C. From Fig. 2D, we clearly identify two Fermi pockets, which touch each other at two discrete zero-dimensional points, that is, two nodes, located on the opposite sides of the k_y axis. Figure 2F shows the constant energy contour at $E_B = 25$ meV of the same region. We see that the upper pocket expands, whereas the lower pocket shrinks upon changing the binding energy from $E_B = 0$ to 25 meV. This demonstrates that the upper pocket is hole-like, whereas the lower one is electron-like. Therefore, the two nodes observed in Fig. 2D are touching points between the electron and hole pockets. We now study the band dispersion away from the touching points along different momentum space cut directions. Figure 2 (B, D, and F) shows that the observed node arises from the crossing between two bands and that these two bands disperse linearly away from the node along all three k directions. Moreover, although the Fermi velocities of the two bands have the opposite signs along the k_x and k_z directions, they have the same sign along the k_y direction.

Now, on the basis of the established results in topological band theory, we show how our systematic data provide decisive evidence for the type II Weyl fermions. Our experimental demonstration below does not depend on the agreement between ARPES data and band structure calculations. Our data show (i) that the conduction and valence bands cross each other, (ii) that the crossing points are zero-dimensional, and (iii) that the bands disperse linearly away from the node along all three k directions (k_x , k_y , k_z). Therefore, the observed crossing points are either Dirac or Weyl nodes. Dirac nodes can only exist in systems with

both time-reversal and space-inversion symmetries (45). Moreover, as exhaustively classified by topological band theory (45), a Dirac node can only occur at a high-symmetry point or along a rotational axis in the bulk BZ. By contrast, Weyl nodes can only exist in systems, which either breaks time-reversal or space-inversion symmetry (4, 5). Topological band theory shows that they occur at generic k points because they are accidental band degeneracies, which do not require any additional crystalline symmetry beyond translation (1, 4, 5). In our case, the LaAlGe crystal breaks inversion symmetry, as reported in previous works (41–43) and also further confirmed by our XRD data (see section S1). Moreover, the k space coordinate of observed crossing point is $(\pm 0.022 \frac{2\pi}{a}, \pm 0.47 \frac{2\pi}{b}, \pm 0.82 \frac{2\pi}{c})$. This is obviously a generic k point, which does not coincide with any high symmetry point or rotational axis. These systematic data demonstrate that the observed band crossings are the Weyl nodes but are not sufficient to distinguish between types I and II, which is the main focus of our paper. We now proceed to prove the type II character based on its definition. Type I Weyl fermions have a typical conical dispersion, and their Fermi surface consists of isolated points, the Weyl nodes. Type II Weyl fermions manifest as tilted-over cones. Their Fermi surface consists of a hole pocket and an electron pocket touching at points, the type II Weyl nodes (19). Along the tilting direction, the Fermi velocities of the two bands that form the Weyl cone are of the same sign, whereas along the other two directions perpendicular to the tilting direction, the Fermi velocities are of opposite signs. Our data on the Fermi surface (Fig. 2D), the constant energy contour (Fig. 2F), and the energy dispersions along all three k directions (Fig. 3 B, D, and F) provide all the decisive evidence, as described above. Therefore, we have unambiguously and clearly shown the type II Weyl fermions in LaAlGe. The decisive experimental proof without relying on data-calculation agreement achieved here is in sharp contrast with the ARPES works on $W_{1-x}Mo_xTe_2$ (32–38). The theoretical predictions of the type II Weyl fermion state in $W_{1-x}Mo_xTe_2$ and LaAlGe have already been well established by first-principles calculations. Hence, showing some data feature in agreement with calculations and arguing for the experimental observation based on such an agreement go little beyond the calculation/prediction itself. Calculations do not account for sample quality issues. Thus, only an experimental observation independent of data-calculation agreement can demonstrate that the sample quality enters the regime where the predicted novel physics is present in real materials.

On the basis of our data, we can quantify the amount of Lorentz symmetry breaking and fully characterize the Weyl fermions observed in LaAlGe. From our ARPES data, we can directly obtain the Fermi velocities of the two bands that form the Weyl cone along the following momentum space directions: (100), (010), (001), (110), (101), and (011). For example, we denote the Fermi velocities of the two bands along the (100) direction as $v_{\pm(100)}$. We show that these data allow us to obtain systematically quantitative information of the Weyl cones. Using these Fermi velocities, we define a three-vector $\mathbf{v} = (v_1, v_2, v_3)$, where $v_1 = \frac{v_{+(100)} + v_{-(100)}}{2}$ and the definitions for v_2 and v_3 follows. We also define a 3×3 matrix \hat{U} whose components are $U_{1,1} = (v_{+(100)} - v_{-(100)})^2/4$ as well as $U_{1,2} = [(v_{+(110)} - v_{-(110)})^2 - (v_{+(100)} - v_{-(100)})^2 - (v_{+(010)} - v_{-(010)})^2]/8$, and the definitions of the other components will follow. Using \mathbf{v} and \hat{U} , one can reconstruct the full low-energy dispersion $\epsilon(\mathbf{k})$ by $\epsilon(\mathbf{k}) = \mathbf{k}^T \mathbf{v} \pm \sqrt{\mathbf{k}^T \hat{U} \mathbf{k}}$ as well as the Berry curvature $\Omega(\mathbf{k}) = \pm \mathbf{k} \det \hat{U} / (\mathbf{k}^T \hat{U} \mathbf{k})^{3/2}$. Finally, the type of the Weyl cone is determined by the eigenvalues of the 3×3 matrix $\hat{U} - \mathbf{v}\mathbf{v}^T$ (19): If all eigenvalues of this matrix are positive, then the Weyl cone is type I, otherwise it is type II.

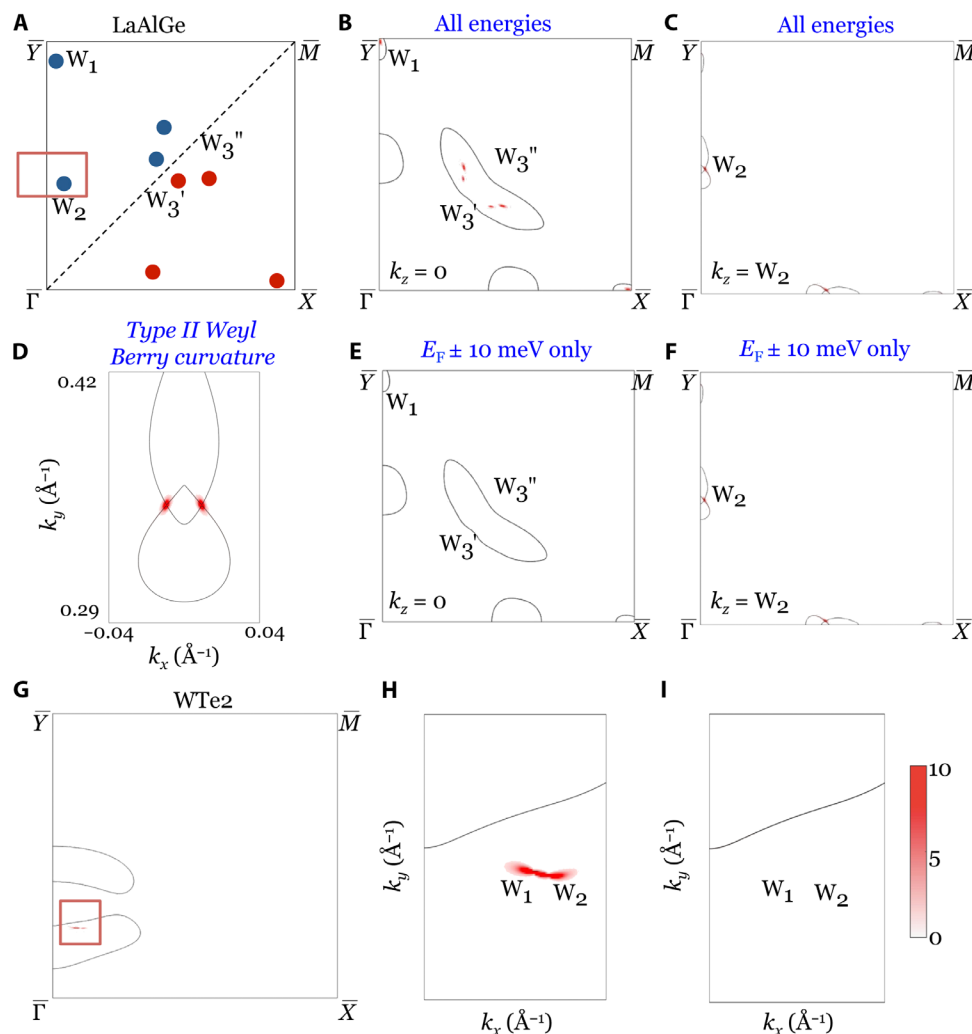


Fig. 4. Berry curvature contributions from the Weyl nodes. (A) Projection of the Weyl nodes of LaAlGe on the (001) surface BZ in one quadrant. (B and C) Berry curvature magnitude in $k_x - k_y$ space at two different k_z values ($k_z = 0$ and $k_z = W_2$) summed over a wide energy range. Specifically, we summed up Berry curvature contributions of all the valence bands, from the lowest valence band near the Fermi level to the highest valence band far from the Fermi level. (E and F) Same as (B) and (C) but only for energies very close to the Fermi level at an E_F of a ± 10 -meV window. (D) A zoomed-in view of the Berry curvature magnitude near the energy of the W_2 Weyl nodes. (G) Berry curvature magnitude in $k_x - k_y$ space summed over a wide energy range in WTe₂. The black lines show the Fermi surface contours. We see significant Berry curvature contribution due to the existence of Weyl nodes. (H) A zoomed-in view of (G) in the k range highlighted by the orange box. (I) Same as (H) for energies close to the Fermi level in an E_F of a ± 10 -meV window window. Because the Weyl nodes are far (50 meV) away from the Fermi level, when we only consider the Fermi level, we do not see any significant Berry curvature.

Using our ARPES data, we can determine

$$\mathbf{v} = (0.32, -1, 71, -0.32) \text{eV} \cdot \text{\AA},$$

$$\hat{U} = \begin{pmatrix} 2.36 & -0.73 & -0.68 \\ -0.73 & 1.40 & -0.15 \\ -0.68 & -0.15 & 0.94 \end{pmatrix} \text{eV}^2 \cdot \text{\AA}^2 \quad (1)$$

The eigenvalues of $\hat{U} - \mathbf{v}\mathbf{v}^T$ are **2.46**, **-1.74**, and **0.85 eV²·Å²**, which again proves the type II nature of the Weyl nodes. This precise information about the low-energy effective theory will, for example, be important to analyze the anomalous transport response of Weyl semimetals sourced by the the Berry curvature around the Weyl node.

The above experimental demonstration and quantitative characterization of the type II Weyl fermions in LaAlGe are only based on our

systematic experimental data and established results in topological band theory. We did not rely on any agreement between data and calculations. We now compare our data and calculations in Figs. 2 and 3. All the critical properties including the Fermi surface (Figs. 2, D and E), the constant energy contour (Fig. 2, F and G), and the energy dispersions along all three \mathbf{k} directions (Fig. 3, B to G) are qualitatively consistent between data and calculations. We emphasize that the bulk band structure calculations, unlike the surface-state calculations, do not have free parameters and therefore are quite reliable. The agreement between our data and calculations provide further strong support on our conclusions.

We also present $\mathbf{k}_x - \mathbf{k}_y$ Fermi surface data at a different photon energy, which corresponds to the \mathbf{k}_z value of the W_1 , W_3' , and W_3'' Weyl nodes ($\mathbf{k}_z = 0$). Figure 2 (H and I) show the calculated and measured Fermi surfaces at $\mathbf{k}_z = 0$, respectively. We observe three types

of pockets, a small pocket near each BZ boundary, a trapezoid-shaped pocket along each diagonal (45°) direction, and a circular pocket in between two adjacent trapezoidal pockets. The data (Fig. 2I) and calculation (Fig. 2H) are in good agreement. From the calculations, we know that the small pocket near the boundary arises from a pair of nearby W_1 Weyl fermions, and the trapezoid-shaped pocket arises from pairs of W_3' and W_3'' Weyl fermions. Because the energy of the W_1 , W_3' , and W_3'' Weyl nodes are far above the Fermi level, the constant energy contour at the Fermi level already merges into a single pocket and hence does not carry net chiral charge.

We show that the type II Weyl nodes dominate the low-energy Berry curvature physics. The color plots in Fig. 4 (B and C) show the Berry curvature magnitude in $k_x - k_y$ space at the two different k_z values. We note that Fig. 4 (B and C) considers the Berry curvature magnitude summed over contributions from a wide energy range. It can be seen that the Berry curvature is indeed dominated by the contribution from the Weyl nodes. By contrast, the trivial pocket at $k_z = \mathbf{0}$ has no observable Berry curvature contribution. To understand the low-energy Berry curvature physics, which can be measured by certain transport experiments such as the negative longitudinal magnetoresistance, we need to know the Berry curvature in close vicinity of the Fermi energy. In Fig. 4 (E and F), we again show the Berry curvature magnitude but only considering the contribution near the Fermi level within a ± 10 -meV window. We see that the Fermi pockets that arise from W_1 and W_3' (W_3'') Weyl cones (Fig. 4E) do not carry observable Berry curvature near the Fermi level. On the other hand, Fermi pockets that arise from the type II Weyl cones (Fig. 4E) show strong Berry curvature in the vicinity of the W_2 Weyl nodes. This is quite intuitive. Because the Weyl nodes are monopoles, the Berry curvature decays rapidly as $\frac{1}{E^2}$ away from the energy of the node. Therefore, the Fermi pockets from W_1 and W_3' (W_3'') Weyl cones show negligibly small Berry curvature contribution. We prove that the type II Weyl nodes dominate the low-energy Berry curvature physics, which dictates topological phenomena such as the negative longitudinal magnetoresistance and the nonlocal transport due to the chiral anomaly (10, 11).

DISCUSSIONS

We discuss the distinction between LaAlGe and the $W_{1-x}Mo_xTe_2$ systems. Current experimental searching for the type II Weyl fermions has been focused on the $W_{1-x}Mo_xTe_2$ system (19–22, 32–38). Most works tried to study the surface states in connection to the Fermi arcs (32–38). However, the surface Fermi arcs cannot discern whether the bulk Weyl fermions are of type I or type II. Huang *et al.* (32) argued the existence of Weyl nodes by normalizing the 6-eV ARPES spectrum taken at high temperature with a Fermi Dirac distribution. As we explained in Fig. 3 (J to M), the projected band structure without k_z resolution cannot distinguish a type II Weyl node in the bulk BZ (Fig. 3K) from a projected trivial crossing between a trivial electron and a trivial hole pocket. Moreover, the type II Weyl nodes in $W_{1-x}Mo_xTe_2$ is quite far away (~ 50 meV) from the chemical potential. By contrast, our systematic ARPES data on LaAlGe provide the clear and direct observation of the type II Weyl fermions. The type II Weyl nodes in LaAlGe are located exactly at the Fermi level, and their Berry curvatures dominate at the Fermi level. Finally, we suggest that one could engineer the chemical potential by chemically doping LaAlGe. For example, both $La_{1-x}Ce_xAlGe$ and $LaAl_{1-x}Ge_{1+x}$ may electron dope the system, by which we may be able to move the chemical potential to the W_1 , W_3' , or W_3'' Weyl nodes. This may give rise to a transition

from a type II to a type I Weyl semimetal in an engineered LaAlGe system.

MATERIALS AND METHODS

High-quality single crystals of LaAlGe were grown by the flux method (46). The SX-ARPES measurements were performed at the ADDRESS Beamline at the Swiss Light Source, Paul Scherrer Institute in Villigen, Switzerland. The experimental geometry of SX-ARPES has been described in the study of Strocov *et al.* (47). The sample was cooled down to 12 K to quench the electron-phonon interaction effects, reducing the k -resolved spectral fraction. The SX photon energy ranged from 300 to 1000 eV. The combined (beamline and analyzer) experimental energy resolution of the SX-ARPES varied between 40 and 80 meV. The angular resolution of the SX-ARPES analyzer was 0.07° . High-resolution vacuum ultraviolet ARPES measurements were performed using the synchrotron radiation light source-based ARPES instruments at Beamline 10.0.1 of the Advanced Light Source (ALS) at the Lawrence Berkeley National Laboratory in Berkeley, CA. The energy and momentum resolution of the vacuum ultraviolet ARPES instruments were better than 30 meV and 1% of the surface BZ. Samples were cleaved in situ under a vacuum condition better than 5×10^{-11} torr.

The first-principles calculations were performed within the density functional theory (48) framework with the projector augmented wave basis, using the Vienna ab initio simulation package (49, 50). The Perdew-Burke-Ernzerhof type generalized gradient approximation was used to describe the exchange-correlation energy (51). A plane wave cutoff of 320 eV was used, and an $8 \times 8 \times 8$ k -mesh was chosen to sample the bulk BZ. The total energies were converged to 10^{-8} eV. SOC was taken into account self-consistently to treat relativistic effects. The experimentally measured lattice constants, $a = b = 4.344$ Å and $c = 14.812$ Å, determined from our own XRD measurements were used to compute the bulk band structures. To calculate the surface states, we constructed a first-principle tight-binding model Hamiltonian. The real-space tight-binding Hamiltonian was constructed using the Wannier function method with La s, d, f ; Al s, p ; and Ge s, p orbitals (52). We calculated the surface spectral weight of semi-infinite (001) slab of LaAlGe using Green's function method.

SUPPLEMENTARY MATERIALS

Supplementary material for this article is available at <http://advances.sciencemag.org/cgi/content/full/3/6/e1603266/DC1>

- section S1. Additional methods
- section S2. Full characterization of the type II Weyl fermions in LaAlGe
- section S3. Decisive evidence for type II Weyl fermions
- section S4. The importance of measuring the band structure along all three k (k_x, k_y, k_z) directions and the issues in $W_{1-x}Mo_xTe_2$
- section S5. Topological definition of Fermi arc surface states and its implications for surface states in LaAlGe and $W_{1-x}Mo_xTe_2$
- section S6. Surface-state band structure of LaAlGe
- section S7. Fermi arc surface states associated with the W_2 Weyl nodes in LaAlGe
- section S8. Fermi arc surface states associated with the W_3' and W_3'' Weyl nodes
- section S9. Topological definition of Fermi arc surface states and its implications for surface states in LaAlGe and $W_{1-x}Mo_xTe_2$
- table S1. Energy dispersive spectroscopy (EDS) data.
- table S2. ARPES-measured Fermi velocities near W_2 .
- table S3. Calculated Fermi velocities near W_2 .
- fig. S1. Energy-dispersive x-ray spectroscopy of LaAlGe samples.
- fig. S2. XRD data of LaAlGe.
- fig. S3. Low-energy electron diffraction data of LaAlGe taken at 100-eV electron energy.
- fig. S4. The 40 Weyl nodes in LaAlGe.

fig. S5. A comparison between the Fermi arcs in type I and type II Weyl semimetals, demonstrating that the Fermi arcs (the green line) cannot be used to discern between type I and type II Weyl fermions.

fig. S6. A comparison between a true crossing in the bulk band structure and a “projected” crossing in the projected band structure.

fig. S7. The presence of projected crossing in the projected band structure of WTe₂ even when the bulk has no Weyl nodes.

fig. S8. Definition of the topological Fermi arc surface states.

fig. S9. Bulk band structure and its projection onto the surface in LaAlGe.

fig. S10. TaAs surface Fermi surface calculations under three different surface onsite potential values.

fig. S11. Band structure of WTe₂ under two slightly different lattice constant values.

fig. S12. A side-by-side comparison of the main data figures between our work and the two W_{1-x}Mo_xTe₂ works (32, 37).

fig. S13. Fermi arc-like and Fermi arc-derived surface states in LaAlGe.

fig. S14. Fermi arc-like and Fermi arc-derived surface states in LaAlGe.

fig. S15. Fermi arc surface states associated with the W₃' and W₃" Weyl nodes.

fig. S16. Connectivity pattern of the Fermi arcs associated with the W₃' and W₃" Weyl nodes.

References (53, 54)

REFERENCES AND NOTES

- C. Herring, Accidental degeneracy in the energy bands of crystals. *Phys. Rev.* **52**, 365–373 (1937).
- H. Weyl, Elektron und gravitation. I. *Z. Phys.* **56**, 330–352 (1929).
- G. E. Volovik, *The Universe in a Helium Droplet* (Clarendon Press, 2003).
- S. Murakami, Phase transition between the quantum spin Hall and insulator phases in 3D: Emergence of a topological gapless phase. *New J. Phys.* **9**, 356 (2007).
- X. Wan, A. M. Turner, A. Vishwanath, S. Y. Savrasov, Topological semimetal and Fermi-arc surface states in the electronic structure of pyrochlore iridates. *Phys. Rev. B* **83**, 205101 (2011).
- A. A. Burkov, L. Balents, Weyl semimetal in a topological insulator multilayer. *Phys. Rev. Lett.* **107**, 127205 (2011).
- S.-Y. Xu, I. Belopolski, N. Alidoust, M. Neupane, G. Bian, C. Zhang, R. Sankar, G. Chang, Z. Yuan, C.-C. Lee, S.-M. Huang, H. Zheng, J. Ma, D. S. Sanchez, B. Wang, A. Bansil, F. Chou, P. P. Shibayev, H. Lin, S. Jia, M. Zahid Hasan, Discovery of a Weyl fermion semimetal and topological Fermi arcs. *Science* **349**, 613–617 (2015).
- L. Lu, Z. Wang, D. Ye, L. Ran, L. Fu, J. D. Joannopoulos, M. Soljačić, Experimental observation of Weyl points. *Science* **349**, 622–624 (2015).
- B. Q. Lv, H. M. Weng, B. B. Fu, X. P. Wang, H. Miao, J. Ma, P. Richard, X. C. Huang, L. X. Zhao, G. F. Chen, Z. Fang, X. Dai, T. Qian, H. Ding, Experimental discovery of Weyl semimetal TaAs. *Phys. Rev. X* **5**, 031013 (2015).
- T. Parameswaran, T. Grover, D. A. Abanin, D. A. Pesin, A. Vishwanath, Probing the chiral anomaly with nonlocal transport in three-dimensional topological semimetals. *Phys. Rev. X* **4**, 031035 (2014).
- H. B. Nielsen, M. Ninomiya, The Adler-Bell-Jackiw anomaly and Weyl fermions in a crystal. *Phys. Lett. B* **130**, 389–396 (1983).
- H. A. Lorentz, La théorie électromagnétique de Maxwell et son application aux corps mouvants. *Arch. Néerlandaises* **52**, 363–552 (1892).
- D. Mattingly, Modern tests of Lorentz invariance. *Living Rev. Relativ.* **8**, 5 (2005).
- V. A. Kostelecký, N. Russell, Data tables for Lorentz and CPT violation. *Rev. Mod. Phys.* **83**, 11–31 (2011).
- N. Russell, Framing Lorentz symmetry (2004); <http://cerncourier.com/cws/article/cern/29224>.
- A. G. Grushin, Consequences of a condensed matter realization of Lorentz violating QED in Weyl semi-metals. *Phys. Rev. D* **86**, 045001 (2012).
- Y. Xu, F. Zhang, C. Zhang, Structured Weyl points in spin-orbit coupled fermionic superfluids. *Phys. Rev. Lett.* **115**, 265304 (2015).
- E. J. Bergholtz, Z. Liu, M. Trescher, R. Moessner, M. Udagawa, Topology and interactions in a frustrated slab: Tuning from Weyl semimetals to $C > 1$ fractional Chern insulators. *Phys. Rev. Lett.* **114**, 016806 (2015).
- A. A. Soluyanov, D. Gresch, C. Wang, Q. Wu, M. Troyer, X. Dai, B. A. Bernevig, Type II Weyl semimetals. *Nature* **527**, 495–498 (2015).
- Y. Sun, S.-C. Wu, M. N. Ali, C. Felser, B. Yan, Prediction of the Weyl semimetal in the orthorhombic MoTe₂. *Phys. Rev. B* **92**, 161107(R) (2015).
- T.-R. Chang, S.-Y. Xu, G. Chang, C.-C. Lee, S.-M. Huang, B. Wang, G. Bian, H. Zheng, D. S. Sanchez, I. Belopolski, N. Alidoust, M. Neupane, A. Bansil, H.-T. Jeng, H. Lin, M. Zahid Hasan, Prediction of an arc-tunable Weyl Fermion metallic state in Mo_xW_{1-x}Te₂. *Nat. Commun.* **7**, 10639 (2016).
- Z. Wang, D. Gresch, A. A. Soluyanov, W. Xie, S. Kushwaha, X. Dai, M. Troyer, R. J. Cava, B. A. Bernevig, MoTe₂: A type-II Weyl topological metal. *Phys. Rev. Lett.* **117**, 056805 (2016).
- G. Chang, S.-Y. Xu, D. S. Sanchez, S.-M. Huang, C.-C. Lee, T.-R. Chang, G. Bian, H. Zheng, I. Belopolski, N. Alidoust, H.-T. Jeng, A. Bansil, H. Lin, M. Zahid Hasan, A strongly robust type II Weyl fermion semimetal state in Ta₃S₂. *Sci. Adv.* **2**, e1600295 (2016).
- K. Koepnick, D. Kasinathan, D. V. Efremov, S. Khim, S. Borisenko, B. Büchner, J. van den Brink, TaIrTe₄: A ternary type-II Weyl semimetal. *Phys. Rev. B* **93**, 201101(R) (2016).
- G. Autès, D. Gresch, M. Troyer, A. A. Soluyanov, O. V. Yazyev, Robust type-II Weyl semimetal phase in transition metal diphosphides XP₂ (X = Mo, W). *Phys. Rev. Lett.* **117**, 066402 (2016).
- A. A. Zyuzin, R. P. Tiwari, Intrinsic anomalous Hall effect in type-II Weyl semimetals. *JETP Lett.* **103**, 717–722 (2016).
- T. E. O'Brien, M. Diez, C. W. J. Beenakker, Magnetic breakdown and Klein tunneling in a type-II Weyl semimetal. *Phys. Rev. Lett.* **116**, 236401 (2016).
- Z.-M. Yu, Y. Yao, S. A. Yang, Predicted unusual magnetoresponse in type-II Weyl semimetals. *Phys. Rev. Lett.* **117**, 077202 (2016).
- M. Udagawa, E. J. Bergholtz, Field-selective anomaly and chiral charge reversal in type-II Weyl materials. *Phys. Rev. Lett.* **117**, 086401 (2016).
- S. Tchoumakov, M. Civelli, M. O. Goerbig, Magnetic-field-induced relativistic properties in type-I and type-II Weyl semimetals. *Phys. Rev. Lett.* **117**, 086402 (2016).
- C.-K. Chan, Y.-T. Oh, J. H. Han, P. A. Lee, Type-II Weyl cone transitions in driven semimetals. *Phys. Rev. B* **94**, 121106(R) (2016).
- L. Huang, T. M. McCormick, M. Ochi, Z. Zhao, M.-T. Suzuki, R. Arita, Y. Wu, D. Mou, H. Cao, J. Yan, N. Trivedi, A. Kaminski, Spectroscopic evidence for type II Weyl semimetal state in MoTe₂. *Nat. Mater.* **15**, 1155–1160 (2016).
- Y. Wu, D. Mou, N. H. Jo, K. Sun, L. Huang, S. L. Bud'ko, P. C. Canfield, A. Kaminski, Observation of Fermi arcs in type-II Weyl semimetal candidate WTe₂. *Phys. Rev. B* **94**, 121113(R) (2016).
- C. Wang, Y. Zhang, J. Huang, S. Nie, G. Liu, A. Liang, Y. Zhang, B. Shen, J. Liu, C. Hu, Y. Ding, D. Liu, Y. Hu, S. He, L. Zhao, L. Yu, J. Hu, J. Wei, Z. Mao, Y. Shi, X. Jia, F. Zhang, S. Zhang, F. Yang, Z. Wang, Q. Peng, H. Weng, X. Dai, Z. Fang, Z. Xu, C. Chen, X. J. Zhou, Spectroscopic evidence of type II Weyl semimetal state in WTe₂. *Phys. Rev. B* **94**, 241119 (2016).
- K. Deng, G. Wan, P. Deng, K. Zhang, S. Ding, E. Wang, M. Yan, H. Huang, H. Zhang, Z. Xu, J. Denlinger, A. Fedorov, H. Yang, W. Duan, H. Yao, Y. Wu, S. Fan, H. Zhang, X. Chen, S. Zhou, Experimental observation of topological Fermi arcs in type-II Weyl semimetal MoTe₂. *Nat. Phys.* **12**, 1105–1110 (2016).
- J. Jiang, Z. K. Liu, Y. Sun, H. F. Yang, C. R. Rajamathi, Y. P. Qi, L. X. Yang, C. Chen, H. Peng, C.-C. Huang, S. Z. Sun, S.-K. Mo, I. Vobornik, J. Fujii, S. S. P. Parkin, C. Felser, B. H. Yan, Y. L. Chen, Signature of type-II Weyl semimetal phase in MoTe₂. *Nat. Commun.* **8**, 13973 (2017).
- A. Liang, J. Huang, S. Nie, Y. Ding, Q. Gao, C. Hu, S. He, Y. Zhang, C. Wang, B. Shen, J. Liu, P. Ai, L. Yu, X. Sun, W. Zhao, S. Lv, D. Liu, C. Li, Y. Zhang, Y. Hu, Y. Xu, L. Zhao, G. Liu, Z. Mao, X. Jia, F. Zhang, S. Zhang, F. Yang, Z. Wang, Q. Peng, H. Weng, X. Dai, Z. Fang, Z. Xu, C. Chen, X. J. Zhou, Electronic Evidence for Type II Weyl Semimetal State in MoTe₂. <http://arxiv.org/abs/1604.01706> (2016).
- N. Xu, Z. J. Wang, A. P. Weber, A. Magrez, P. Bugnon, H. Berger, C. E. Matt, J. Z. Ma, B. B. Fu, B. Q. Lv, N. C. Plumb, M. Radovic, E. Pomjakushina, K. Conder, T. Qian, J. H. Dil, J. Mesot, H. Ding, M. Shi, Discovery of Weyl semimetal state violating Lorentz invariance in MoTe₂. <http://arxiv.org/abs/1604.02116> (2016).
- X. Huang, L. Zhao, Y. Long, P. Wang, D. Chen, Z. Yang, H. Liang, M. Xue, H. Weng, Z. Fang, X. Dai, G. Chen, Observation of the chiral anomaly induced negative magneto-resistance in 3D Weyl semi-metal TaAs. *Phys. Rev. X* **5**, 031023 (2015).
- C.-L. Zhang, S.-Y. Xu, I. Belopolski, Z. Yuan, Z. Lin, B. Tong, G. Bian, N. Alidoust, C.-C. Lee, S.-M. Huang, T.-R. Chang, G. Chang, C.-H. Hsu, H.-T. Jeng, M. Neupane, D. S. Sanchez, H. Zheng, J. Wang, H. Lin, C. Zhang, H.-Z. Lu, S.-Q. Shen, T. Neupert, M. Zahid Hasan, S. Jia, Signatures of the Adler-Bell-Jackiw chiral anomaly in a Weyl fermion semimetal. *Nat. Commun.* **7**, 10735 (2016).
- A. M. Guloy, J. D. Corbett, Syntheses and structures of lanthanum germanide, LaGe₂-x, and lanthanum aluminum germanide, LaAlGe: Interrelationships among the alpha-ThSi₂, alpha-GdSi₂, and LaPtSi structure types. *Inorg. Chem.* **30**, 4789–4794 (1991).
- J. T. Zhao, E. Parthé, Structure of YAlGe and isotopic rare-earth-aluminium germanides. *Acta Crystallogr.* **46**, 2276–2279 (1990).
- A. Raman, H. Steinrück, Crystal chemistry of AB₂ structures. I. Investigations on AB₂ sections in the ternary systems rare earth-aluminum-silicon, -germanium, and -tin. *Inorg. Chem.* **6**, 1789–1791 (1967).
- V. N. Strocov, M. Kobayashi, X. Wang, L. L. Lev, J. Krempasky, V. V. Rogalev, T. Schmitt, C. Cancellieri, M. L. Reinle-Schmitt, Soft-X-ray ARPES at the Swiss Light Source: From 3D materials to buried interfaces and impurities. *Synch. Rad. News* **27**, 31–40 (2014).
- B.-J. Yang, N. Nagaosa, Classification of stable three-dimensional Dirac semimetals with nontrivial topology. *Nat. Commun.* **5**, 4898 (2014).
- S. Bobev, P. H. Tobash, V. Fritsch, J. D. Thompson, M. F. Hundley, J. L. Sarrao, Z. Fisk, Ternary rare-earth aluminosilicides—Single-crystal growth from Al flux, structural and physical properties. *J. Solid State Chem.* **178**, 2091–2103 (2005).

47. V. N. Strocov, X. Wang, M. Shi, M. Kobayashi, J. Krempasky, C. Hess, T. Schmitt, L. Patthey, Soft-X-ray ARPES facility at the ADDRESS beamline of the SLS: Concepts, technical realisation and scientific applications. *J. Synchrotron Radiat.* **21**, 32–44 (2014).
48. P. Hohenberg, W. Kohn, Inhomogeneous electron gas. *Phys. Rev.* **136**, B864–B871 (1964).
49. G. Kresse, J. Furthmüller, Efficient iterative schemes for *ab initio* total-energy calculations using a plane-wave basis set. *Phys. Rev. B* **54**, 11169–11186 (1996).
50. G. Kresse, D. Joubert, From ultrasoft pseudopotentials to the projector augmented-wave method. *Phys. Rev. B* **59**, 1758–1775 (1999).
51. J. P. Perdew, K. Burke, M. Ernzerhof, Generalized gradient approximation made simple. *Phys. Rev. Lett.* **77**, 3865–3868 (1996).
52. N. Marzari, D. Vanderbilt, Maximally localized generalized Wannier functions for composite energy bands. *Phys. Rev. B* **56**, 12847–12865 (1997).
53. A. C. Potter, I. Kimchi, A. Vishwanath, Quantum oscillations from surface Fermi arcs in Weyl and Dirac semimetals. *Nat. Commun.* **5**, 5161 (2014).
54. A. A. Yanaki, V. A. Obolonchik, Preparation of transition-metal tellurides by means of hydrogen telluride. *Inorg. Mater.* **9**, 1855–1858 (1973).
55. A. Mar, S. Jobic, J. A. Ibers, Metal-metal vs tellurium-tellurium bonding in WTe_2 and its ternary variants TaIrTe_4 and NbIrTe_4 . *J. Am. Chem. Soc.* **114**, 8963–8971 (1992).

Acknowledgments: We acknowledge J. D. Denlinger, S. K. Mo, A. V. Fedorov, M. Hashimoto, M. Hoesch, T. Kim, and V. N. Strocov for their beamline assistance at the ALS, the Stanford Synchrotron Radiation Lightsource, the Diamond Light Source, and the Swiss Light Source. We also thank D. Huse, I. Klebanov, A. Polyakov, P. Steinhardt, H. Verlinde, and A. Vishwanath for discussions. H. Lin acknowledges visiting scientist support from Princeton University.

Funding: Work at Princeton University and Princeton-led synchrotron-based ARPES measurements were supported by the Gordon and Betty Moore Foundation EPIQS Initiative through (grant GBMF4547 to M.Z.H.). Single-crystal growth was supported by the National Basic Research Program of China (grant nos. 2013CB921901 and 2014CB239302), and characterization was supported by the U.S. Department of Energy (DE-FG-02-05ER46200). First-principles band structure calculations at the National University of Singapore were supported by the National Research Foundation (NRF), Prime Minister's Office, Singapore under its NRF fellowship (NRF award no. NRF-NRFF2013-03). The work at Northeastern

University was supported by the U.S. Department of Energy (DOE), Office of Science, Basic Energy Sciences grant number DE-FG02-07ER46352, and benefited from Northeastern University's Advanced Scientific Computation Center (ASCC) and the NERSC supercomputing center through DOE grant number DE-AC02-05CH11231. M.-A.H. was supported by the Swiss Excellence Scholarship Grant ESKAS-No. 2015.0257. T.-R.C. and H.-T.J. are supported by the Ministry of Science and Technology, the National Tsing Hua University, the National Cheng Kung University, and the Academia Sinica, Taiwan. T.-R.C. and H.-T.J. also thank the National Center for High-performance Computing, the Computer and Information Networking Center-National Taiwan University, and the National Center for Theoretical Sciences, Taiwan for technical support. H.-T.J. received funding from the Ministry of Science and Technology, Taiwan (103-2112-M-007 -018 -MY3) from 1 August 2014 to 31 July 2017. **Author contributions:** S.-Y.X., N.A., I.B., D.S.S., G.B., and H.Z. conducted the ARPES experiments with assistance from M.-A.H., V.N.S., and M.Z.H. H. Lu, X.Z., Y.B., and S.J. grew the single-crystal samples. G.C., B.S., S.-M.H., C.-H.H., T.-R.C., H.-T.J., A.B., and H. Lin performed first-principles band structure calculations. T.N. did theoretical analyses. M.Z.H. was responsible for the overall direction, planning, and integration among different research units. **Competing interests:** The authors declare that they have no competing interests. **Data and materials availability:** All data needed to evaluate the conclusions in the paper are present in the paper and/or the Supplementary Materials. Additional data related to this paper may be requested from M.Z.H. (mzhasan@princeton.edu).

Submitted 2 February 2017

Accepted 7 April 2017

Published 2 June 2017

10.1126/sciadv.1603266

Citation: S.-Y. Xu, N. Alidoust, G. Chang, H. Lu, B. Singh, I. Belopolski, D. S. Sanchez, X. Zhang, G. Bian, H. Zheng, M.-A. Husanu, Y. Bian, S.-M. Huang, C.-H. Hsu, T.-R. Chang, H.-T. Jeng, A. Bansil, T. Neupert, V. N. Strocov, H. Lin, S. Jia, M. Z. Hasan, Discovery of Lorentz-violating type II Weyl fermions in LaAlGe . *Sci. Adv.* **3**, e1603266 (2017).

Discovery of Lorentz-violating type II Weyl fermions in LaAlGe

Su-Yang Xu, Nasser Alidoust, Guoqing Chang, Hong Lu, Bahadur Singh, Ilya Belopolski, Daniel S. Sanchez, Xiao Zhang, Guang Bian, Hao Zheng, Marius-Adrian Husanu, Yi Bian, Shin-Ming Huang, Chuang-Han Hsu, Tay-Rong Chang, Horng-Tay Jeng, Arun Bansil, Titus Neupert, Vladimir N. Strocov, Hsin Lin, Shuang Jia and M. Zahid Hasan

Sci Adv **3** (6), e1603266.
DOI: 10.1126/sciadv.1603266

ARTICLE TOOLS

<http://advances.sciencemag.org/content/3/6/e1603266>

SUPPLEMENTARY MATERIALS

<http://advances.sciencemag.org/content/suppl/2017/05/26/3.6.e1603266.DC1>

REFERENCES

This article cites 51 articles, 3 of which you can access for free
<http://advances.sciencemag.org/content/3/6/e1603266#BIBL>

PERMISSIONS

<http://www.sciencemag.org/help/reprints-and-permissions>

Use of this article is subject to the [Terms of Service](#)

Science Advances (ISSN 2375-2548) is published by the American Association for the Advancement of Science, 1200 New York Avenue NW, Washington, DC 20005. 2017 © The Authors, some rights reserved; exclusive licensee American Association for the Advancement of Science. No claim to original U.S. Government Works. The title *Science Advances* is a registered trademark of AAAS.